ACS APPLIED BIO MATERIALS

www.acsabm.org

Article

Infrared-Activated Bactericide: Rhenium Disulfide (ReS_2)-Functionalized Mesoporous Silica Nanoparticles

Ha Na, Melissa Venedicto, Chen-Yu Chang, Jake Carrier, and Cheng-Yu Lai*

Cite This: *ACS Appl. Bio Mater.* 2023, 6, 1577−1585

Read Online

ACCESS | Metrics & More | Article Recommendations | Supporting Information

ABSTRACT: An attractive strategy for treating bacterial infection is the combination of antibiotic chemotherapy with photothermal therapy (PTT), which could be implemented using multifunctional nanomaterials. In this work, the intrinsic photothermal efficiency of two-dimensional (2D) rhenium disulfide (ReS_2) nanosheets is enhanced by their coating on mesoporous silica nanoparticles (MSNs) to realize a highly efficient light-responsive nanoparticle endowed with controlled-release drug delivery capability, denoted as MSN-ReS_2. The MSN component of the hybrid nanoparticle features augmented pore size toward facilitating increased loading of antibacterial drugs. The ReS_2 synthesis is conducted in the presence of MSNs through an *in situ* hydrothermal reaction and leads to a uniform surface coating of the nanosphere. The MSN-ReS_2 bactericide testing showed more than 99% bacterial killing efficiency in both Gram-negative bacteria (*Escherichia coli*) and Gram-positive bacteria (*Staphylococcus aureus*) upon laser irradiation. A cooperative effect that led to a 100% bactericide effect on Gram-negative bacteria (*E. coli*) was observed when tetracycline hydrochloride was loaded in the carrier. The results show the potential of MSN-ReS_2 to be used as a wound-healing therapeutic with a synergistic bactericide role.

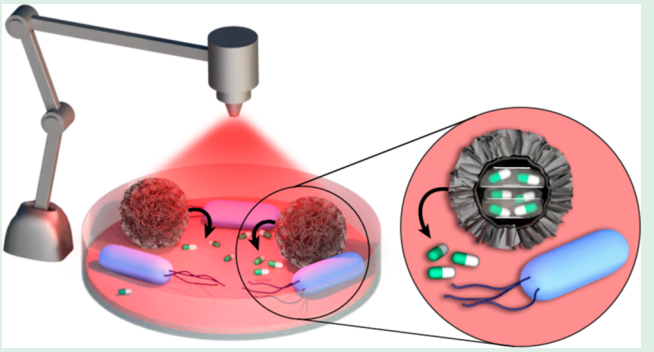

KEYWORDS: *mesoporous silica nanoparticles, ReS_2, bactericide, photothermal, antibacterial*

1. INTRODUCTION

Wound healing, used by the body to repair damaged tissue, is a homeostatic process that occurs after an injury or rupture of the skin.[1] Although most small skin damages heal without external intervention, large full-thickness skin defects, where wounds are usually deeper and more severe than superficial ones, could result in severe inflammatory responses and are prone to bacterial infections, which require medical treatment.[2] Antibiotics are the most widely used form of chemotherapy for bacterial infections, but the overuse and abuse of antibiotics can induce bacterial resistance, often culminating with the development of super-bacteria (bacteria resistant to one or more antibiotics).[3,4] As the development of new antibiotics is both expensive and time-consuming, therapeutic nanomaterials with antibacterial and antioxidant properties emerged as potent wound-healing alternatives.[5−11] Specifically, the atomically thin two-dimensional transition metal dichalcogenides (2D TMDCs) could interact with bacteria both chemically and physically, thus reducing microbes' ability to develop antibiotic resistance. For example, molybdenum disulfide (MoS_2) nanosheets exhibit antimicrobial activity, which could be explained both by MoS_2 affinity for water, potentially leading to cell membrane disruption, and by the dichalcogenide's property to generate reactive oxygen species (ROS) when exposed to light.[12,13] Furthermore, poly(ethylene glycol)-functionalized molybdenum disulfide nanoflowers (PEG-MoS_2 NFs) showed a 95% inhibition rate of two tetracycline-resistant bacterial strains when irradiated with an 808 nm near-infrared (NIR) laser.[14]

The outstanding photothermal properties of various 2D materials could bring synergy to the bacterial eradication process and have seen increased interest in recent years. Near-infrared (NIR) light features higher energy of photons relative to UV light as well as less scattering and absorption in biological tissues, and therefore IR lasers are the key choice for photothermal therapy (PTT) applications. In addition to being minimally invasive to noninvasive, PTT using near-infrared (NIR) irradiation enables deep tissue penetration depth and does not pose the challenge of nondrug resistance, thus having great potential in the antibacterial and antitumor therapy arena.[15−18] Owing to their outstanding optoelectronic properties, strong light−matter interactions, prominent excitonic effects, large surface area, and reduced dimensionality, 2D

Received: December 30, 2022
Accepted: February 13, 2023
Published: February 20, 2023

TMDCs are at the forefront of many other applications.[19−21] Combined with their good biocompatibility and strong NIR absorption, TMDCs have been investigated as potential photothermal agents.[22−27] One promising TMDC is ReS_2, which has been shown to possess excellent photothermal capabilities and good biocompatibility.[28−30] ReS_2 exhibits photothermal properties and has been employed for cancer therapy as theranostic *in vitro* when treated with a NIR laser.[30,31]

Multifunctional nanomaterials open avenues to combine antibiotic chemotherapy with photothermal therapy (PTT) in a system that includes a drug nanocarrier and a 2D TMDC. Compared with traditional drug carriers such as liposomes and emulsions, inorganic carriers demonstrated a significant role in the biomedical field due to their excellent stability, facile surface functionalization, and unique optical, magnetic, electrical, and physical properties.[32] Among them, mesoporous silica nanoparticles (MSNs) serve not only general inorganic carrier functions but further benefit from adjustable pore size, large surface area, and tunable yet narrow particle size distribution.[32−38] By functionalizing their surface or using their pores as a reservoir for the control-releasing of desired cargo molecules, MSNs can serve as a versatile platform for various biomedical applications.[39−42]

In this work, we designed and tested a multifunctional bactericide system consisting of the MSN nanoparticle with expanded pore size and 2D TMDC rhenium disulfide (ReS_2) gating nanosheets that serve as both antibacterial and photothermal agents. The expanded pores facilitate the loading of an antibiotic, tetracycline hydrochloride. The photothermal efficiency of MSN-ReS_2 was measured. The antibacterial properties of MSN-ReS_2 were evaluated by the spread plate method, fluorescence probe staining, and electron microscopy, demonstrating that MSN- ReS_2 possesses good stability and dispersity. The system features an unprecedented photothermal conversion efficiency (28.7%), 100% of tetracycline hydrochloride loading capacity, and over 99% of the bacterial killing effect when tested in vitro. The results suggest the potential of MSN-ReS_2 in bactericide and wound-healing biomedical applications.

2. EXPERIMENTAL SECTION

2.1. Materials. Hexadecyltrimethylammonium bromide (CTAB, ≥99%) was purchased from Sigma-Aldrich (Saint Louis, MI). Tetraethyl orthosilicate (TEOS, 99.9%) was purchased from Alfa Aesar (Haverhill, MA). Mesitylene (99%), hydrochloric acid (HCl, 37%), hydroxylamine hydrochloride ($NH_2OH{\cdot}HCl$, 99 + %), thiourea (99%), ammonium perrhenate (VII) (NH_4ReO_4, 99 + %), tetracycline hydrochloride (TC), sodium hydroxide (NaOH), sodium chloride (NaCl), acridine orange (AO), glutaraldehyde (50%), and methanol were purchased from ThermoFisher Scientific (Waltham, MA). Propidium iodide (PI) was purchased from Biotium (Fremont, CA). Ethanol (200 proof, 100% by volume) was purchased from Decon Labs (King of Prussia, PA). ACS reagent-grade nanopure water was purchased from LabChem (Zelienople, PA). LB broth (Lennox L Broth) and LB agar (Lennox L Agar) were purchased from Research Products International (Mount Prospect, IL). Phosphate-buffered saline (PBS, pH 7.4) without calcium and magnesium was purchased from Lonza Bioscience (Walkersville, MD). All chemicals were used without further purification unless otherwise indicated.

2.2. Characterization. Nanoparticle imaging was performed with a JEOL/JSM-F100 Schottky field emission scanning electron microscope (FE-SEM) and a ThermoFisher Talos/F200X scanning transmission microscope (STEM) to determine the particle size and morphology. ζ Potentials were measured on a Malvern/Zetasizer Nano-ZSZEN3600 operated at room temperature. The specific surface areas of the materials were determined *via* nitrogen adsorption−desorption isothermal curves using Brunauer−Emmett−Teller (BET) theory on a Quantachrome/NOVAtouch LX-2; the density functional theory (DFT) method was used to determine the pore volume and pore size distribution. Fourier transform infrared spectroscopy (FT-IR) was conducted on a Shimadzu/IRTracer-100 to validate the removal of the surfactant template. UV absorption spectroscopy was employed for a UV−visible spectrophotometer (Thermo Scientific/BioMate 160). X-ray diffraction (XRD) measurements were performed on a Rigaku MiniFlex600 equipped with Cu Kα radiation (λ = 1.5405 Å) operating at 40 mV and 30 mA. Raman spectroscopy was performed with a confocal Raman microscope (WITec alpha300 R) using a 532 nm laser. Fluorescent properties were analyzed using a Nikon C2 laser scanning confocal microscope system. An 808 nm NIR laser (RLDH808-1200-5, Roithner Laserthchnik Gmbh, Vienna, Austria) was used for the photothermal therapy study. The temperature of the solution was recorded with a TH-5 Thermalert Clinical Monitoring Thermometer (Physitemp Instruments, Clifton, NJ). A heated stage insert (World Precision Instruments Inc.) was used to hold the cell culture plates at 37 °C.

2.3. Synthesis of Expanded Pore-Sized Mesoporous Silica Nanoparticles (MSNs). Mesoporous silica nanoparticles were prepared according to a previously described procedure.[43] In a typical experiment, CTAB (2.00 g, 5.48 mmol) was added to a solution obtained by dissolving NaOH (0.56 g, 14.0 mmol) in nanopure water (480 mL). This mixture was heated under stirring and kept at 85 °C to ensure complete dissolution of CTAB. After 1.5 h, 14 mL of mesitylene (0.90 g, 7.42 mmol) was added to the mixed solution and stirred for another 3 h. Subsequently, 10 mL of TEOS (9.33 g, 44.8 mmol) was added swiftly into the mixture and continuously stirred for 2.5 h. The resulting white suspension (MSNs-CTAB) was isolated by filtration of the hot suspension. The filtrate was washed three times with nanopure water and twice with methanol, followed by drying overnight in a vacuum oven. To remove the surfactant template (CTAB), 1.50 g of MSNs-CTAB nanoparticles was refluxed for 24 h at 75 °C in a solution formed of 160 mL of methanol and 9 mL of HCl (37%) (18:1 v/v). The resulting MSNs were isolated *via* filtration of the hot suspension. The filtrate was washed three times with nanopure water and twice with methanol, followed by drying overnight in a vacuum oven.

2.4. Synthesis of ReS_2-Coated MSNs (MSN-ReS_2) and ReS_2. An amount of 0.200 g of MSNs prepared as described in Section 2.3 was dispersed in 20 mL of nanopure water and ultrasonicated for 20 min, resulting in an opaque (milky) suspension. Separately, a solution of NH_4ReO_4 (0.161 g, 0.600 mmol), $NH_2OH{\cdot}HCl$ (0.125 g, 1.80 mmol), and thiourea (0.205 g, 2.70 mmol) was prepared in 50 mL of nanopure water.[35] The mixture was stirred overnight at room temperature (12 h) and then transferred in a tightly sealed autoclave which was introduced in a box furnace heated at 240 °C and allowed to react for 24 h. Upon reaction, the autoclave was cooled at room temperature, and the product was collected by centrifugation at 4000 rpm for 30 min. The resulting nanoparticles were washed three times with nanopure water, collected by centrifugation, and dried in a vacuum oven. Similarly, ReS_2 was synthesized by the same procedure without the addition of MSNs.

2.5. Photothermal Properties of MSN-ReS_2. MSN-ReS_2 suspensions (300 μL in nanopure water) with different concentrations (0, 10, 25, 50, 100, 200, 400, 800 $\mu g{\cdot}mL^{-1}$) were placed in 2 mL test tubes and irradiated for 10 min with an 808 nm NIR laser (Roithner Lasertechnik GmbH/RLDH808-1200-5) using a laser power density of 1 $W{\cdot}cm^{-2}$. The temperature of the solution was recorded every 10 s by a digital thermometer (Physitemp/TH-5) connected with a high-temperature microprobe thermocouple. The MSN-ReS_2 suspension with a fixed concentration of 200 $\mu g{\cdot}mL^{-1}$ was irradiated with the same 808 nm NIR laser for 10 min; next, the laser was shut off for measuring the cooling temperature; the temperature was recorded every 60 s until the suspension reached room temperature.[44] The photothermal conversion efficiency was calculated according to previously reported methods.[45,46]

https://doi.org/10.1021/acsabm.2c01084
ACS Appl. Bio Mater. 2023, 6, 1577−1585

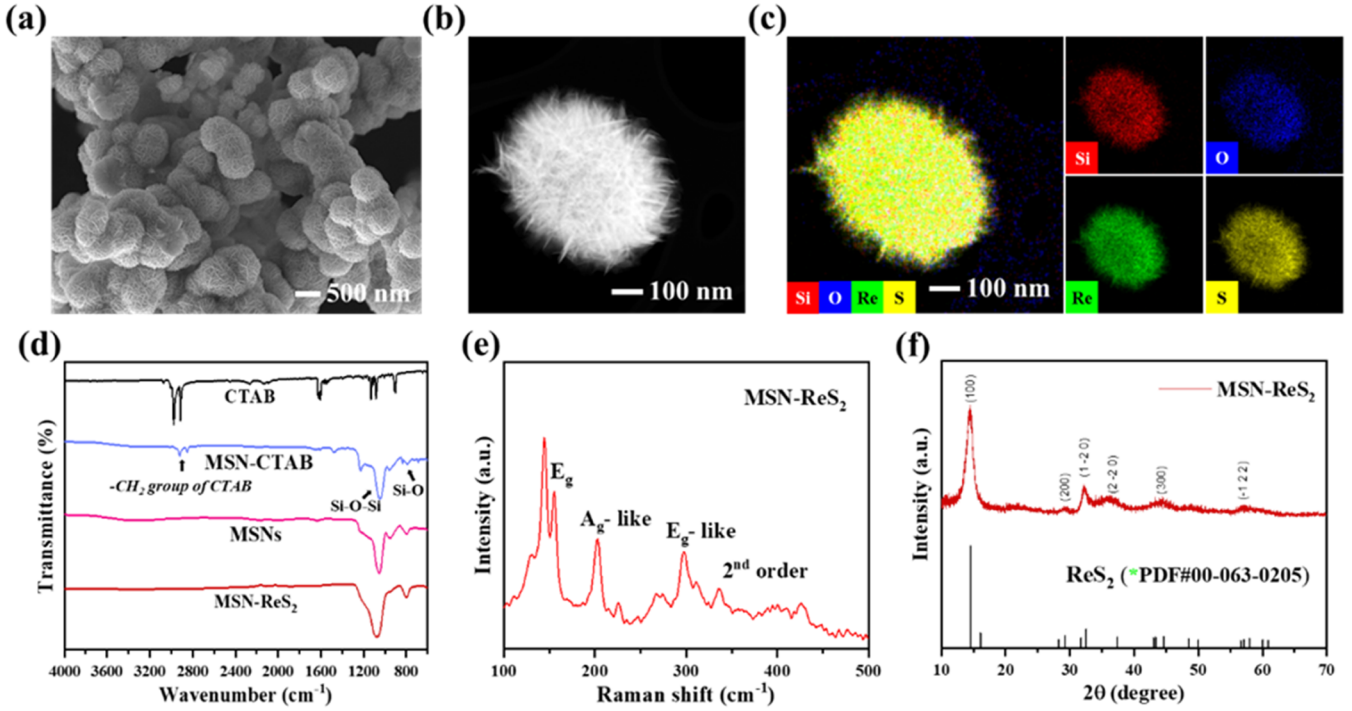

Figure 1. MSN-ReS_2 nanoparticle characterization results: (a) FE-SEM showing the particle morphology; (b) STEM showing the size and shape of an MSN-ReS_2 nanoparticle; (c) STEM-EDS images validating the presence of all elements of ReS_2 and MSN (Re, S, Si, and O); (d) FT-IR; (e) Raman spectra; and (f) XRD patterns.

2.6. Loading of Tetracycline Hydrochloride (TC) and Determination of Loading Efficiency (LE). Predetermined amounts of MSNs and MSN-ReS_2 nanoparticles were dispersed into nanopure water by ultrasonication for 20 min. Tetracycline hydrochloride (TC) was prepared as a 1 mg·mL^{-1} aqueous solution under ultrasonication for 15 min. The nanoparticles were dispersed in the TC aqueous solution at a 1:10 ratio (TC/nanoparticles mass ratio). After stirring in the dark at room temperature for 24 h to allow the drug uploading, the nanoparticles were collected by high-speed centrifugation, which served both to isolate the loaded carrier and to remove the unloaded antibiotic. The drug-loaded nanoparticles were collected upon freeze-drying in a lyophilizer at −80 °C for 24 h. The nanoparticle loading efficiency (LE) was determined by UV−vis spectroscopy using a calibration curve (Figure S9, Supporting Information) raised by measuring the absorption curve of TC (0.1, 0.05, 0.025, 0.0125, 0.00625, and 0.0 mg·mL^{-1}) at λ_{max} = 357 nm using eq 1.

$$\text{LE}\ (\%) = \frac{\text{weight of loaded drug(mg)}}{\text{weight of drug used for loading (mg)}} \times 100 \quad (1)$$

2.7. Cumulative Drug Release of MSN-ReS_2. The quantification of TC release from MSN-ReS_2 was conducted in PBS buffer (pH 7.4). In a typical experiment, 10 mg of MSN-ReS_2/TC was dispersed into 2 mL of PBS buffer and placed in the dark. After one hour, the supernatant was collected by centrifugation at 10,000 rpm for 5 min. The supernatant's absorbance was measured with a UV−vis spectrophotometer at λ_{max} = 357 nm. Next, the resulting pellet was redispersed into pH 7.4 buffer and the same steps were followed to determine the release amount at 2, 4, 6, 8, 12, 24, and 48 h. The cumulative release profile was determined using the TC calibration curve and calculating the concentration of the drug released over time.

2.8. Bacterial Culture. *Escherichia coli* (*E. coli*, ATCC3 35218, KWIK-STIK) and *Staphylococcus aureus* (*S. aureus*, ATCC 29213, KWIK-STIK) were cultured in a liquid Luria−Bertani (LB) culture medium kept at 37 °C, shaken at 170 rpm overnight, and harvested at the logarithmic growth phase before the experiments. The concentration of the bacteria was controlled by measuring the optical density at a wavelength of 600 nm (OD 600) using a UV−vis spectrophotometer.

2.9. *In Vitro* Bactericide Evaluation. The antibacterial effect of nanoparticles on *E. coli* and *S. aureus* was evaluated using the spread plate method.[47] Briefly, the bacteria were collected by centrifugation at 10,000 rpm for 3 min and washed with PBS to remove the culture medium. Next, the PBS (pH 7.4) bacterial resuspension (*E. coli* and *S. aureus*) was added into 2 mL test tubes in the following twelve groups: (1) control: bacteria + PBS; (2) bacteria + MSN; (3) bacteria + MSN/TC; (4) bacteria + ReS_2; (5) bacteria + MSN-ReS_2; (6) bacteria + MSN-ReS_2/TC; (7) bacteria + PBS + NIR 808 nm; (8) bacteria + MSN + NIR 808 nm; (9) bacteria + MSN/TC + NIR 808 nm; (10) bacteria + ReS_2 + NIR 808 nm; (11) bacteria + MSN-ReS_2 + NIR 808 nm; and (12) bacteria + MSN-ReS_2/TC + NIR 808 nm. The groups of (7)−(12) were further exposed to an NIR laser (808 nm, 1.0 W·cm^{-2}) for 10 min. The final concentrations of samples and bacteria were 200 μg·mL^{-1} and 1.0 × 10^6 colony forming units (CFU)·mL^{-1}, respectively. The total volume of solution in each well was 300 μL. After incubation for 4 h, 100 μL of the bacterial suspension of groups (1)−(12) were diluted 1000-fold, spread on an agar culture plate, and incubated at 37 °C for 17 h. Each experiment was performed in triplicate and the number of colonies was counted. The bacteria survival rate was calculated using eq 2.

$$\text{viability}(\%) = \frac{\#\ \text{of colonies formed in exp. group}}{\#\ \text{of colonies formed in control group}} \times 100 \quad (2)$$

2.10. Viability Staining Test. An amount of 100 μL of the 1.0 × 10^8 CFU·mL^{-1} bacterial suspension (*E. coli* and *S. aureus*) was washed with 0.85% NaCl after the above irradiation and incubation and then costained with 4.0 μM AO and 8.0 μM PI at 37 °C in the dark for 1 h. Next, 5 μL of the above mixture was dropped onto an 18 × 18 mm cover glass. A confocal fluorescence microscope was used for imaging, measuring the green (live) and red (dead) fluorescence signals at 488 and 561 nm, respectively.

2.11. Imaging of Bacterial Morphology. For SEM imaging, each bacterial specimen was prepared as follows. The bacteria suspensions (*E. coli* and *S. aureus*) (100 μL, 1.0 × 10^8 CFU·mL^{-1})

https://doi.org/10.1021/acsabm.2c01084
ACS Appl. Bio Mater. 2023, 6, 1577−1585

were centrifuged (4000 rpm, 3 min) and redispersed into glutaraldehyde (2.5% in PBS) for fixation after antibacterial treatments. After 24 h, the fixed samples were dehydrated using 500 μL of a gradient ethanol solution with increasing concentration (10, 30, 50, 70, 90, and 100% ethanol) for 10 min each.[47] Next, each bacterial suspension was resuspended in 15 μL of ethanol and dropped on a 9 mm circular cover glass and further dried in air. The circular cover glass samples were taped to the sample holder and sputter-coated with Au to obtain a coating of ∼5 nm Au thickness. Each sample was imaged by SEM at 15.0 kV.

2.12. Statistical Analysis. All collected data were tabulated and the mean ± standard deviation (SD) was calculated for each data set. The analysis of these experimental groups was compared by Student's multiple *t*-test, by which $p < 0.05$ (*), $p < 0.01$ (**), and $p < 0.001$ (***) were regarded as statistically significant.

3. RESULTS AND DISCUSSION

3.1. Nanomaterial Particle Size and Morphology. MSN nanoparticles with an expanded pore size were synthesized following literature-reported procedures[43,48] and employed as a supporting scaffold for the ReS_2 *in situ* hydrothermal synthesis.[49,50] FE-SEM imaging shows an MSNs average diameter of ∼300 nm (Figure S1). Also, MSNs featured pore size with ∼5 nm diameter mesopores in the silica framework, as shown by high-resolution transmission electron microscopy (HRTEM) (Figure S2). After ReS_2 coating, the resulting MSN-ReS_2 hybrid nanoparticles show an average diameter of ∼400 to 500 nm by FE-SEM (Figure 1a) and DLS (Figure S18, Supporting Information), and the ReS_2 nanosheets in the MSN-ReS_2 (Figure 1a,b) show similar morphology and aggregation as the stand-alone ReS_2 nanosheets (Figures S3 and S4).

FT-IR spectroscopy displays silicon dioxide characteristic absorption peaks at 1050 and 798 cm^{-1} attributed to the vibration of Si−O−Si and Si−O, respectively (Figure 1d). The C−N stretching vibration peak at 1471 cm^{-1} corresponding to CTAB disappeared in the MSN framework, indicating that the CTAB template was removed successfully after the acid wash procedure.

Raman spectroscopy (Figure 1e) was employed to validate the presence and purity of ReS_2, showing two characteristic Raman modes at 155.6 and 206.9 cm^{-1} resulting from the in-plane (E_g) and mostly out-of-plane (A_g-like) vibrational modes of ReS_2, respectively. Also, E_g and 2nd-order vibrational modes arise due to the low crystal symmetry.[51]

Low-angle powder XRD patterns of MSNs (Figure S4) showed a characteristic MSN peak $2\theta°$ of 1.65°, which belongs to the d_{100} diffraction lattice plane of ordered hexagonal pore structures.[52] The presence of the two additional characteristic diffraction peaks located at $2\theta = 2.79°$ and $2\theta = 3.22°$ corresponding to the diffraction surface index of (110) and (200), respectively, indicate that the long-range order of the pore structure was significantly enhanced after an acid wash. For ReS_2-coated MSNs and 240 °C hydrothermal-treated MSNs, the MSN characteristic diffraction peaks (Figure S4) owing to the ordered porosity were not observed, suggesting structural changes due to the hydrothermal treatment. However, sharp diffraction peaks appeared at $2\theta = 14.32°$ and $2\theta = 32.26°$ (Figure 1f), attributed to the (100) and (002) diffraction index of triclinic ReS_2 consistent with (PDF#00-063-0205) validating the crystallinity of ReS_2 coating.

3.2. Porosity Testing. To confirm that the pores are accessible both before and after coating, we employed nitrogen physisorption measurements. The MSN shows a type-IV nitrogen adsorption−desorption isotherm with capillary condensation in the range of $P/P_0 = 0.3-1.0$, pointing to a cylindrical pore structure characteristic of the mesoporous materials. The pore size distribution (Figure S6b) further confirmed that the pore size within the MSN sample was relatively uniform. The material has an average pore size of 5.09 nm, as calculated by the density functional theory (DFT) method and volume analysis, and a large surface area of 1013 $m^2 \cdot g^{-1}$, as determined by the Brunauer−Emmett−Teller (BET) surface area analysis method (Table 1).[53] After being coated with ReS_2 (Figure S7), the nitrogen adsorption−desorption isotherm showed an H3-type hysteresis loop, which may be considered as the slit hole of the accumulation of ReS_2 sheets and did not exhibit adsorption saturation in the range of higher relative pressure. The average surface area and pore sizes were 76.3 $m^2 \cdot g^{-1}$ and 6.5 nm, respectively, after DFT and BET calculations.

Table 1. BET Characterization Results for MSNs and MSN-ReS_2

nanoparticles	pore size (nm)	surface area ($m^2 \cdot g^{-1}$)
MSNs	5.09	1013
MSN-ReS_2	6.49	76.3

3.3. Photothermal Response. The MSN-ReS_2 and ReS_2 aqueous solutions with different concentrations (0, 10, 25, 50, 100, 200, 400, 800 $\mu g \cdot mL^{-1}$) were irradiated continuously with an 808 nm NIR laser for 10 min and the temperature increase was recorded by a microprobe inserted into the dispersion. Nanopure water was used as a negative control. As shown in Figure S8, increasing MSN-ReS_2 and ReS_2 concentrations lead to a temperature change (ΔT) increase.

As shown in Figure 2a,b, the temperature of the MSN-ReS_2 (200 $\mu g \cdot mL^{-1}$) aqueous solution could rapidly raise up to 63.4 °C with a temperature increase of 42.8 °C ($\Delta T_{max,dispersion}$), which was 12.1 °C higher than ReS_2 (200 $\mu g \cdot mL^{-1}$) and much higher than the negative control for 3.9 °C ($\Delta T_{max,H_2O}$). After 10 min of irradiation, the NIR laser was shut off and the temperature was recorded for another 17 min, as shown in Figure 2b.

The photothermal conversion efficiency (η) was calculated according to eq 3.[45]

$$\eta = \frac{hA(\Delta T_{max,dispersion} - \Delta T_{max,\ H_2O})}{I(1 - 10^{-A_\lambda})} \quad (3)$$

where h is the heat transfer coefficient, A is the surface area of the container, $\Delta T_{max,dispersion}$ and $\Delta T_{max,H_2O}$ are the temperature change of MSN-ReS_2 and solvent water at the maximum steady-state temperature, respectively, I is the laser power, and A_λ is the absorbance of MSN-ReS_2 at 808 nm in aqueous solution. The A_λ was obtained by averaging triplicate measurements. The calculated photothermal conversion efficiency (η) of MSN-ReS_2 was 28.7%, larger than the η of stand-alone ReS_2, which was calculated as 22%. All materials employed in this work were tested for photothermal stability and demonstrated that after five cycles of irradiation, ReS_2, MSN-ReS_2, and MSN-ReS_2-TC all show consistent performance, indicating their high photothermal stability (Supporting Information, Figures S16 and S17).

3.4. Synergetic In Vitro Chemotherapy and PTT. As a broad-spectrum antibiotic, which mainly inhibits bacterial

https://doi.org/10.1021/acsabm.2c01084
ACS Appl. Bio Mater. 2023, 6, 1577−1585

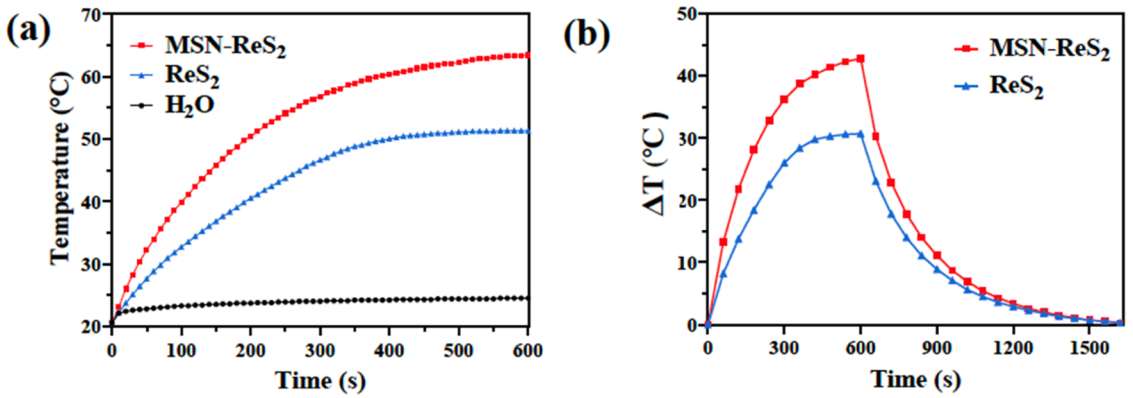

Figure 2. (a) Photothermal heating curves of MSN-ReS_2 (200 $\mu g \cdot mL^{-1}$), ReS_2 (200 $\mu g \cdot mL^{-1}$), and nanopure water irradiated by an 808 nm laser (1 $W \cdot cm^{-2}$, 10 min). (b) Temperature change (ΔT) responses of MSN-ReS_2 (200 $\mu g \cdot mL^{-1}$) and ReS_2 (200 $\mu g \cdot mL^{-1}$) to heating and cooling periods over 27 min.

protein synthesis, TC has been widely applied as a bactericide to wounds. In this work, we aimed to explore if the bactericide activity of MSN-ReS_2 could be further enhanced by TC loading. Tetracycline hydrochloride was chosen as a proof-of-concept antibiotic to prove that MSN-ReS_2 has a loading capacity that could further serve for combined drug and irradiation treatment of wounds. Specifically, TC is soluble in water, enabling fast uploading, and it was estimated that the overall molecular size of ~1.1 nm diameter[54] matches the pore size of MSN. The TC molecules were loaded into MSN-ReS_2 by physisorption and are held inside the pores by noncovalent interactions. The loading efficiency, determined by measuring the UV−vis absorption at λ_{max} = 357 nm, was 47.98% as determined using the calibration curve (Figure S9). To investigate the TC release performance of MSN-ReS_2, the drug-release kinetic behavior was revealed at pH 7.4, 37 °C (body temperature). As shown in Figure 3, the cumulative TC

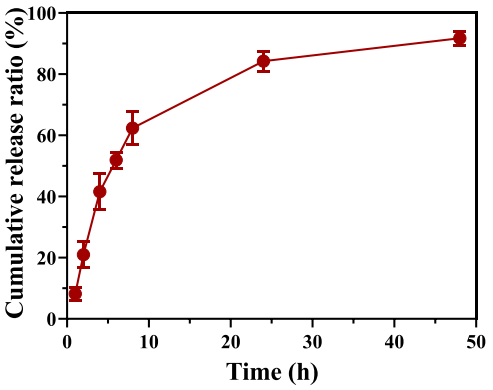

Figure 3. TC release behavior of MSN-ReS_2/TC at 37 °C at pH 7.4.

release ratio at 1, 2, 4, 6, 8, 12, 24, and 48 h was 8.2, 21.0, 41.6, 51.9, 62.4, 84.2, and 91.7%, respectively, demonstrating that MSN-ReS_2 is an effective TC time-release delivery system.

The bactericide effect of MSN-ReS_2 and MSN-ReS_2/TC was evaluated in the presence of the negative control, MSN, MSN/TC, and ReS_2 groups by the spread plate test on *E. coli* (Gram-negative bacteria) and *S. aureus* (Gram-positive bacteria), followed by quantitative analysis. In addition, a control experiment was conducted to capture the antibacterial effect of TC at a concentration equivalent to the one of the TC released from the MSN, showing that irradiation does not impact TC activity. Nevertheless, the TC release is enhanced by 0.74% upon irradiation of MSN-ReS_2-TC in the same conditions (at 37 °C at pH 7.4) (Figure S11, Supporting Information), providing a proof-of-concept for the synergy between irradiation and drug therapy.

As shown in Figure 4a,b, each treatment group without NIR irradiation, as compared with the negative control in the PBS working solution (pH 7.4), showed some intrinsic bactericide effect, especially on *S. aureus* bacteria. However, after irradiation, the ReS_2, MSN-ReS_2, and MSN-ReS_2/TC groups all exhibited an excellent bactericide effect against both *E. coli* and *S. aureus* when compared with the negative control group; this effect is attributed to the photothermal properties of ReS_2. Meanwhile, as shown in Figure 4c,d, the relative viability of the control + NIR group on *E. coli* and *S. aureus* was up to 96.8 and 94.8%, respectively, confirming that the NIR laser itself does not have a significant bactericide effect. For the MSN group, the relative viability of *E. coli* and *S. aureus* was 92.0%. After irradiation, the viability rate decreased to 86.2 and 85.3%, respectively, due to the toxicity of materials and irradiation. For the MSN/TC group, the relative viability of *E. coli* and *S. aureus* was 87.1 and 76.4%. After irradiation, the viability rate decreased to 83.3 and 72.3%, respectively, suggesting a minor synergistic effect between the TC treatment and the effect of irradiation. For the ReS_2 group, the relative viability of *E. coli* and *S. aureus* was 85.9 and 53.5%, which decreased to 0.0 and 6.0% after being treated with NIR laser. In the case of the MSN-ReS_2 group, the rate was 94.6 and 63.4% and decreased to 0.74 and 0.25% after being treated with NIR laser. For the MSN-ReS_2/TC group, the rate was 76.5 and 61.7%, which decreased to 0.0 and 0.17% after being treated with an NIR laser. These results demonstrated that IR-light-activated MSN-ReS_2 has excellent bactericidal activity.

In addition, the bactericidal effect of MSN-ReS_2 was directly observed by conducting live/dead staining (AO and PI) of bacteria after different treatments, and the results were consistent with the spread plate data. As shown in Figure 5a,b, the strong green fluorescence signals in the control, MSN-ReS_2, MSN-ReS_2/TC, and PBS+NIR groups represented the living colonies that could only upload AO. The strong red fluorescence signals in the MSN-ReS_2 + NIR and MSN-ReS_2/TC + NIR groups represent colonies of dead bacteria that could only upload PI. The yellow signals represent the superposition of the green and red fluorescence signals, which could imply that the cell membrane of some bacteria became

https://doi.org/10.1021/acsabm.2c01084
ACS Appl. Bio Mater. 2023, 6, 1577−1585

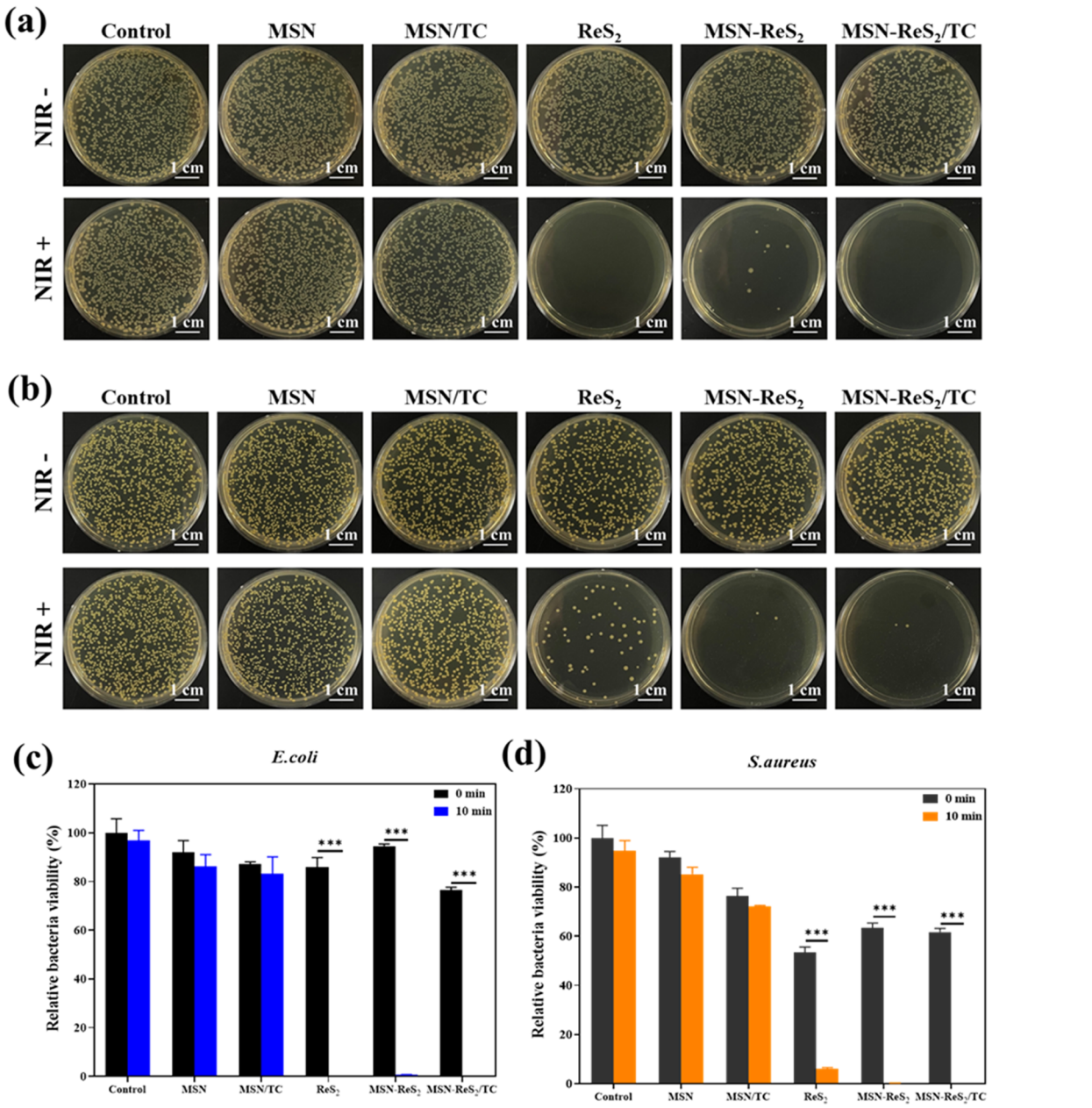

Figure 4. Photographs of the LB agar plates with (a) *E. coli* and (b) *S. aureus* following different treatments. The relative bacterial viability of (c) *E. coli* and (d) *S. aureus* after various treatments based on panels (a and b).

thinner or damaged, thus allowing the PI dye to penetrate the membrane easily, leading to DNA binding and staining the nucleus red.

To further understand the interaction of the hybrid MSN-ReS_2 nanoparticles with bacteria, the morphological changes of bacteria were investigated by SEM. As shown in Figure 5c,d, the antibacterial effects of MSN-ReS_2 and MSN-ReS_2/TC groups were owed to the surface collapse of bacteria, while the bacterial skeleton structure was deformed severely or completely collapsed after 10 min of irradiation. Overall, it was confirmed that the photothermal effect of MSN-ReS_2 hybrid nanoparticles plays a decisive role in the bacteria-killing process, showing great potential as wound bactericide treatment, thus reducing the risk of wound infection.

4. CONCLUSIONS

A hybrid nanoparticle MSN-ReS_2 was fabricated and evaluated for its bactericide effect *in vitro* when irradiated with an NIR (808 nm) laser. Comprehensive characterization of the hybrid nanoparticles revealed ovoidal morphologies and an average particle size of 400−500 nm. The MSN scaffold used for ReS_2 deposition *in situ* preserved porosity (as determined by nitrogen physisorption measurements), but XRD no longer showed the characteristic peak, suggesting either pore obstruction or structural changes. In addition, a significant surface area decrease in MSN-ReS_2 could suggest the collapse of part of the porous structure due to the long hydrothermal synthesis. However, MSN-ReS_2 showed narrow particle size distribution with an average particle size of 400−500 nm (by SEM) and the presence of all elements (Re, S, O, and Si), thus validating the templating effect of the MSN. The *in vitro*

https://doi.org/10.1021/acsabm.2c01084
ACS Appl. Bio Mater. 2023, 6, 1577−1585

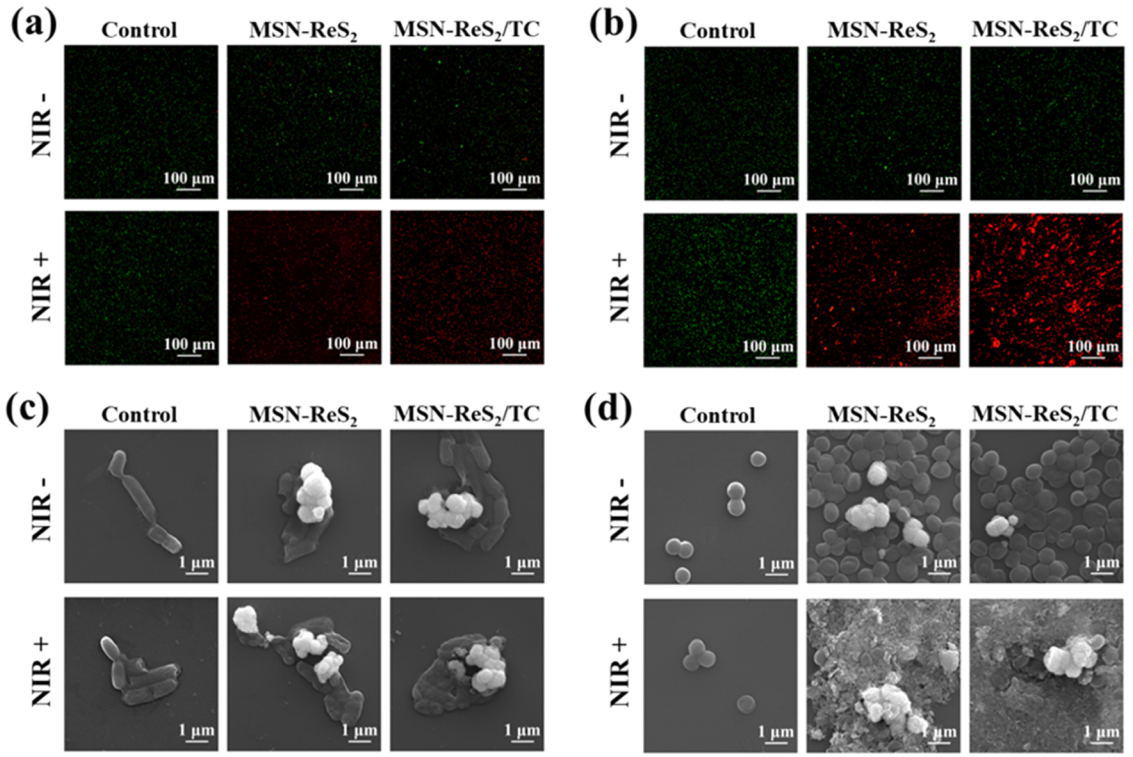

Figure 5. Fluorescence staining merged confocal images of (a) *E. coli* and (b) *S. aureus* using AO/PI for 1 h after different treatments. FE-SEM images of (c) *E. coli* and (d) *S. aureus* after different treatments.

antibacterial evaluation demonstrated that MSN-ReS_2 has an excellent bactericide effect upon irradiation with an NIR laser. The antibiotic drug loading complemented the photothermal response for bacteria killing *in vitro*, showing that antibiotic-loaded MSN-ReS_2 is a potent platform for deep wound healing in synergistic chemo-photothermal therapy.

■ ASSOCIATED CONTENT

Supporting Information

The Supporting Information is available free of charge at https://pubs.acs.org/doi/10.1021/acsabm.2c01084.

Calculation of the photothermal conversion efficiency; FE-SEM and TEM images of MSN; FE-SEM of MSN-ReS_2 and ReS_2; XRD of ReS_2, MSN, and MSN-ReS_2; STEM-EDS analysis of MSN-ReS_2; nitrogen physisorption results; photothermal heating curves of various concentrations of MSN-ReS_2 and ReS_2 irradiated by an 808 nm laser; calibration curve for tetracycline hydrochloride (measured by UV−vis absorbance); photothermal stability of ReS_2, MSN-ReS_2, and MSN-ReS_2-TC; TC release under irradiation; antibacterial effect of TC alone at a concentration equivalent to the one of the TC released from the MSN; TC release from MSN; ReS_2 surface area; UV−vis−NIR absorption spectra of all employed materials; and dynamic light scattering (DLS) characterization of MSN, ReS_2, and MSN-ReS_2 (PDF)

■ AUTHOR INFORMATION

Corresponding Author

Cheng-Yu Lai − *Department of Mechanical and Materials Engineering, Florida International University, Miami 33174, United States; Department of Chemistry and Biochemistry, Florida International University, Miami 33174, United States;* orcid.org/0000-0002-8931-5601; Email: clai@fiu.edu

Authors

Ha Na − *Department of Mechanical and Materials Engineering, Florida International University, Miami 33174, United States;* orcid.org/0000-0003-0872-7231

Melissa Venedicto − *Department of Mechanical and Materials Engineering, Florida International University, Miami 33174, United States;* orcid.org/0000-0001-9413-3653

Chen-Yu Chang − *Department of Mechanical and Materials Engineering, Florida International University, Miami 33174, United States;* orcid.org/0000-0001-5253-1813

Jake Carrier − *Department of Chemistry and Biochemistry, Florida International University, Miami 33174, United States*

Complete contact information is available at: https://pubs.acs.org/10.1021/acsabm.2c01084

Author Contributions

The manuscript was written through contributions of all authors. All authors have given approval to the final version of the manuscript.

Funding

This work was supported in part by the National Science Foundation (NSF) Awards CBET-1924412 and DMR-2122078 and the National Aeronautics and Space Administration (NASA) Award # 80NSSC19M0201.

Notes

The authors declare no competing financial interest.

■ ACKNOWLEDGMENTS

The authors thank Dr. Daniela Radu at Florida International University for valuable discussions, Dr. Anthony McGoron at Florida International University for providing access to the IR laser, and Dr. Ke Wang and Mr. Misra Bharavi at The Pennsylvania State University for assistance with the HRTEM, STEM, and EDX images. Ha Na acknowledges support from an NSF Award DMR-2122078, Melissa Venedicto acknowledges the support from an FIU Presidential Fellowship awarded by the FIU University Graduate School, Chen-Yu Chang acknowledges support from a NASA Award # 80NSSC19M0201, and Jake Carrier acknowledges the support from an FIU Veteran Fellowship awarded by the FIU University Graduate School.

■ REFERENCES

(1) Guo, S.; DiPietro, L. A. Factors affecting wound healing. *J. Dent. Res.* **2010**, *89*, 219−229.
(2) Zeng, W.-N.; Wang, D.; Yu, Q.-P.; Yu, Z.-P.; Wang, H.-Y.; Wu, C.-Y.; Du, S.-W.; Chen, X.-Y.; Li, J.-F.; Zhou, Z.-K. Near-Infrared Light-Controllable Multifunction Mesoporous Polydopamine Nanocomposites for Promoting Infected Wound Healing. *ACS Appl. Mater. Interfaces* **2022**, *14*, 2534−2550.
(3) Feng, Y.; Coradi Tonon, C.; Ashraf, S.; Hasan, T. Photodynamic and antibiotic therapy in combination against bacterial infections: efficacy, determinants, mechanisms, and future perspectives. *Adv. Drug Delivery Rev.* **2021**, *177*, No. 113941.
(4) Xu, X.; Liu, X.; Tan, L.; Cui, Z.; Yang, X.; Zhu, S.; Li, Z.; Yuan, X.; Zheng, Y.; Yeung, K. W. K.; et al. Controlled-temperature photothermal and oxidative bacteria killing and acceleration of wound healing by polydopamine-assisted Au-hydroxyapatite nanorods. *Acta Biomater.* **2018**, *77*, 352−364.
(5) Haghniaz, R.; Rabbani, A.; Vajhadin, F.; Khan, T.; Kousar, R.; Khan, A. R.; Montazerian, H.; Iqbal, J.; Libanori, A.; Kim, H.-J.; Wahid, F. Anti-bacterial and wound healing-promoting effects of zinc ferrite nanoparticles. *J. Nanobiotechnol.* **2021**, *19*, No. 38.
(6) Abdollahi, Z.; Zare, E. N.; Salimi, F.; Goudarzi, I.; Tay, F. R.; Makvandi, P. Bioactive Carboxymethyl Starch-Based Hydrogels Decorated with CuO Nanoparticles: Antioxidant and Antimicrobial Properties and Accelerated Wound Healing In Vivo. *Int. J. Mol. Sci.* **2021**, *22*, No. 2531.
(7) Fu, Y.; Zhang, J.; Wang, Y.; Li, J.; Bao, J.; Xu, X.; Zhang, C.; Li, Y.; Wu, H.; Gu, Z. Reduced polydopamine nanoparticles incorporated oxidized dextran/chitosan hybrid hydrogels with enhanced antioxidative and antibacterial properties for accelerated wound healing. *Carbohydr. Polym.* **2021**, *257*, No. 117598.
(8) Xu, Z.; Liang, B.; Tian, J.; Wu, J. Anti-inflammation biomaterial platforms for chronic wound healing. *Biomater. Sci.* **2021**, *9*, 4388−4409.
(9) Liang, Y.; He, J.; Guo, B. Functional hydrogels as wound dressing to enhance wound healing. *ACS Nano* **2021**, *15*, 12687−12722.
(10) Zeng, Q.; Qi, X.; Shi, G.; Zhang, M.; Haick, H. Wound Dressing: From Nanomaterials to Diagnostic Dressings and Healing Evaluations. *ACS Nano* **2022**, *16*, 1708−1733.
(11) Jia, H.; Zhang, X.; Zeng, X.; Cai, R.; Wang, Z.; Yuan, Y.; Yue, T. Construction of silver nanoparticles anchored flower-like magnetic Fe3O4@SiO2@MnO2 hybrids with antibacterial and wound healing activity. *Appl. Surf. Sci.* **2021**, *567*, No. 150797.
(12) Roy, S.; Mondal, A.; Yadav, V.; Sarkar, A.; Banerjee, R.; Sanpui, P.; Jaiswal, A. Mechanistic Insight into the Antibacterial Activity of Chitosan Exfoliated MoS2 Nanosheets: Membrane Damage, Metabolic Inactivation, and Oxidative Stress. *ACS Appl. Bio Mater.* **2019**, *2*, 2738−2755.
(13) Karunakaran, S.; Pandit, S.; Basu, B.; De, M. Simultaneous Exfoliation and Functionalization of 2H-MoS2 by Thiolated Surfactants: Applications in Enhanced Antibacterial Activity. *J. Am. Chem. Soc.* **2018**, *140*, 12634−12644.
(14) Yin, W.; Yu, J.; Lv, F.; Yan, L.; Zheng, L. R.; Gu, Z.; Zhao, Y. Functionalized Nano-MoS2 with Peroxidase Catalytic and Near-Infrared Photothermal Activities for Safe and Synergetic Wound Antibacterial Applications. *ACS Nano* **2016**, *10*, 11000−11011.
(15) Xu, X.; Fan, M.; Yu, Z.; Zhao, Y.; Zhang, H.; Wang, J.; Wu, M.; Sun, F.; Xu, X.; Ding, C.; et al. A removable photothermal antibacterial "warm paste" target for cariogenic bacteria. *Chem. Eng. J.* **2022**, *429*, No. 132491.
(16) Tan, T.; Wang, H.; Cao, H.; Zeng, L.; Wang, Y.; Wang, Z.; Wang, J.; Li, J.; Wang, S.; Zhang, Z.; Li, Y. Deep Tumor-Penetrated Nanocages Improve Accessibility to Cancer Stem Cells for Photothermal-Chemotherapy of Breast Cancer Metastasis. *Adv. Sci.* **2018**, *5*, No. 1801012.
(17) Tian, S.; Bai, H.; Li, S.; Xiao, Y.; Cui, X.; Li, X.; Tan, J.; Huang, Z.; Shen, D.; Liu, W.; et al. Water-Soluble Organic Nanoparticles with Programable Intermolecular Charge Transfer for NIR-II Photothermal Anti-Bacterial Therapy. *Angew. Chem., Int. Ed.* **2021**, *60*, 11758−11762.
(18) Zhen, W.; Liu, Y.; Lin, L.; Bai, J.; Jia, X.; Tian, H.; Jiang, X. BSA-IrO2: Catalase-like Nanoparticles with High Photothermal Conversion Efficiency and a High X-ray Absorption Coefficient for Anti-inflammation and Antitumor Theranostics. *Angew. Chem., Int. Ed.* **2018**, *57*, 10309−10313.
(19) Mak, K. F.; Shan, J. Photonics and optoelectronics of 2D semiconductor transition metal dichalcogenides. *Nat. Photonics* **2016**, *10*, 216−226.
(20) Manzeli, S.; Ovchinnikov, D.; Pasquier, D.; Yazyev, O. V.; Kis, A. 2D transition metal dichalcogenides. *Nat. Rev. Mater.* **2017**, *2*, No. 17033.
(21) Mueller, T.; Malic, E. Exciton physics and device application of two-dimensional transition metal dichalcogenide semiconductors. *npj 2D Mater. Appl.* **2018**, *2*, No. 29.
(22) Chen, H.; Liu, T.; Su, Z.; Shang, L.; Wei, G. 2D transition metal dichalcogenide nanosheets for photo/thermo-based tumor imaging and therapy. *Nanoscale Horiz.* **2018**, *3*, 74−89.
(23) Chen, Y.; Tan, C.; Zhang, H.; Wang, L. Two-dimensional graphene analogues for biomedical applications. *Chem. Soc. Rev.* **2015**, *44*, 2681−2701.
(24) Cheng, L.; Yuan, C.; Shen, S.; Yi, X.; Gong, H.; Yang, K.; Liu, Z. Bottom-Up Synthesis of Metal-Ion-Doped WS(2) Nanoflakes for Cancer Theranostics. *ACS Nano* **2015**, *9*, 11090−11101.
(25) Gong, L.; Yan, L.; Zhou, R.; Xie, J.; Wu, W.; Gu, Z. Two-dimensional transition metal dichalcogenide nanomaterials for combination cancer therapy. *J. Mater. Chem. B* **2017**, *5*, 1873−1895.
(26) Qian, X.; Shen, S.; Liu, T.; Cheng, L.; Liu, Z. Two-dimensional TiS(2) nanosheets for in vivo photoacoustic imaging and photothermal cancer therapy. *Nanoscale* **2015**, *7*, 6380−6387.
(27) Zhu, Y.; Wang, Y.; Williams, G. R.; Fu, L.; Wu, J.; Wang, H.; Liang, R.; Weng, X.; Wei, M. Multicomponent Transition Metal Dichalcogenide Nanosheets for Imaging-Guided Photothermal and Chemodynamic Therapy. *Adv. Sci.* **2020**, *7*, No. 2000272.
(28) Shen, S.; Chao, Y.; Dong, Z.; Wang, G.; Yi, X.; Song, G.; Yang, K.; Liu, Z.; Cheng, L. Bottom-Up Preparation of Uniform Ultrathin Rhenium Disulfide Nanosheets for Image-Guided Photothermal Radiotherapy. *Adv. Funct. Mater.* **2017**, *27*, No. 1700250.
(29) Miao, Z.; Fan, L.; Xie, X.; Ma, Y.; Xue, J.; He, T.; Zha, Z. Liquid Exfoliation of Atomically Thin Antimony Selenide as an Efficient Two-Dimensional Antibacterial Nanoagent. *ACS Appl. Mater. Interfaces* **2019**, *11*, 26664−26673.
(30) Wang, X.; Wang, J.; Pan, J.; Zhao, F.; Kan, D.; Cheng, R.; Zhang, X.; Sun, S.-K. Rhenium Sulfide Nanoparticles as a Biosafe Spectral CT Contrast Agent for Gastrointestinal Tract Imaging and Tumor Theranostics in Vivo. *ACS Appl. Mater. Interfaces* **2019**, *11*, 33650−33658.
(31) Miao, Z.; Chen, S.; Xu, C.-Y.; Ma, Y.; Qian, H.; Xu, Y.; Chen, H.; Wang, X.; He, G.; Lu, Y.; et al. PEGylated rhenium nanoclusters: a

https://doi.org/10.1021/acsabm.2c01084
ACS Appl. Bio Mater. 2023, 6, 1577−1585

degradable metal photothermal nanoagent for cancer therapy. *Chem. Sci.* **2019**, *10*, 5435−5443.
(32) Choi, G.; Rejinold, N. S.; Piao, H.; Choy, J.-H. Inorganic−inorganic nanohybrids for drug delivery, imaging and photo-therapy: Recent developments and future scope. *Chem. Sci.* **2021**, *12*, 5044−5063.
(33) Kankala, R. K.; Han, Y.-H.; Na, J.; Lee, C.-H.; Sun, Z.; Wang, S.-B.; Kimura, T.; Ok, Y. S.; Yamauchi, Y.; Chen, A.-Z.; Wu, K. C. Nanoarchitectured Structure and Surface Biofunctionality of Mesoporous Silica Nanoparticles. *Adv. Mater.* **2020**, *32*, No. 1907035.
(34) Manzano, M.; Vallet-Regí, M. Mesoporous Silica Nanoparticles for Drug Delivery. *Adv. Funct. Mater.* **2020**, *30*, No. 1902634.
(35) Lai, C.-Y.; Trewyn, B. G.; Jeftinija, D. M.; Jeftinija, K.; Xu, S.; Jeftinija, S.; Lin, V. S.-Y. A mesoporous silica nanosphere-based carrier system with chemically removable CdS nanoparticle caps for stimuli-responsive controlled release of neurotransmitters and drug molecules. *J. Am. Chem. Soc.* **2003**, *125*, 4451−4459.
(36) Lai, C.-Y.; Wu, C.-W.; Radu, D.; Trewyn, B.; Lin, V.-Y. Reversible Binding and Fluorescence Energy Transfer between Surface-Derivatized CdS Nanoparticles and Multi-Functionalized Fluorescent Mesoporous Silica Nanospheres. In *Studies in Surface Science and Catalysis*; Elsevier, 2007; Vol. *170*, pp 1827−1835. DOI: 10.1016/S0167-2991(07)81066-4.
(37) Lin, V. S.-Y.; Lai, C.-Y.; Huang, J.; Song, S.-A.; Xu, S. Molecular recognition inside of multifunctionalized mesoporous silicas: toward selective fluorescence detection of dopamine and glucosamine. *J. Am. Chem. Soc.* **2001**, *123*, 11510−11511.
(38) Radu, D. R.; Lai, C.-Y.; Huang, J.; Shu, X.; Lin, V. S. Y. Fine-tuning the degree of organic functionalization of mesoporous silica nanosphere materials via an interfacially designed co-condensation method. *Chem. Commun.* **2005**, *10*, 1264−1266.
(39) Slowing, I. I.; Vivero-Escoto, J. L.; Wu, C.-W.; Lin, V. S.-Y. Mesoporous silica nanoparticles as controlled release drug delivery and gene transfection carriers. *Adv. Drug Delivery Rev.* **2008**, *60*, 1278−1288.
(40) Hoffmann, F.; Fröba, M. Silica-Based Mesoporous Organic−Inorganic Hybrid Materials. In *The supramolecular chemistry of organic−inorganic hybrid materials*; Wiley: New Jersey, NJ, 2010; pp 39−112 DOI: 10.1002/anie.200503075.
(41) Vallet-Regí, M.; Balas, F.; Arcos, D. Mesoporous materials for drug delivery. *Angew. Chem., Int. Ed.* **2007**, *46*, 7548−7558.
(42) Li, Z.; Barnes, J. C.; Bosoy, A.; Stoddart, J. F.; Zink, J. I. Mesoporous silica nanoparticles in biomedical applications. *Chem. Soc. Rev.* **2012**, *41*, 2590−2605.
(43) Lai, C.-Y.; Trewyn, B. G.; Jeftinija, D. M.; Jeftinija, K.; Xu, S.; Jeftinija, S.; Lin, V. S. Y. A Mesoporous Silica Nanosphere-Based Carrier System with Chemically Removable CdS Nanoparticle Caps for Stimuli-Responsive Controlled Release of Neurotransmitters and Drug Molecules. *J. Am. Chem. Soc.* **2003**, *125*, 4451−4459.
(44) Liu, M.; Radu, D. R.; Selopal, G. S.; Bachu, S.; Lai, C.-Y. Stand-Alone CuFeSe2 (Eskebornite) Nanosheets for Photothermal Cancer Therapy. *Nanomaterials* **2021**, *11*, No. 2008.
(45) Ren, W.; Yan, Y.; Zeng, L.; Shi, Z.; Gong, A.; Schaaf, P.; Wang, D.; Zhao, J.; Zou, B.; Yu, H.; et al. A Near Infrared Light Triggered Hydrogenated Black TiO2 for Cancer Photothermal Therapy. *Adv. Healthcare Mater.* **2015**, *4*, 1526−1536.
(46) Wang, H.; Chang, J.; Shi, M.; Pan, W.; Li, N.; Tang, B. A Dual-Targeted Organic Photothermal Agent for Enhanced Photothermal Therapy. *Angew. Chem., Int. Ed.* **2019**, *58*, 1057−1061.
(47) Wang, X.; Shi, Q.; Zha, Z.; Zhu, D.; Zheng, L.; Shi, L.; Wei, X.; Lian, L.; Wu, K.; Cheng, L. Copper single-atom catalysts with photothermal performance and enhanced nanozyme activity for bacteria-infected wound therapy. *Bioact. Mater.* **2021**, *6*, 4389−4401.
(48) López, V.; Villegas, M. R.; Rodríguez, V.; Villaverde, G.; Lozano, D.; Baeza, A.; Vallet-Regí, M. Janus Mesoporous Silica Nanoparticles for Dual Targeting of Tumor Cells and Mitochondria. *ACS Appl. Mater. Interfaces* **2017**, *9*, 26697−26706.
(49) Moreno-Villaécija, M.-Á.; Sedó-Vegara, J.; Guisasola, E.; Baeza, A.; Regí, M. V.; Nador, F.; Ruiz-Molina, D. Polydopamine-like Coatings as Payload Gatekeepers for Mesoporous Silica Nanoparticles. *ACS Appl. Mater. Interfaces* **2018**, *10*, 7661−7669.
(50) Selamneni, V.; Mukherjee, A.; Raghavan, H.; Gomathi, P. T.; Kolli, C. S. R.; Pal, S.; Hazra, A.; Sahatiya, P. Plasmonic Au Nanoparticles Coated on ReS2 Nanosheets for Visible-Near-Infrared Photodetectors. *ACS Appl. Nano Mater.* **2022**, *5*, 11381−11390.
(51) Tongay, S.; Sahin, H.; Ko, C.; Luce, A.; Fan, W.; Liu, K.; Zhou, J.; Huang, Y.-S.; Ho, C.-H.; Yan, J.; et al. Monolayer behaviour in bulk ReS2 due to electronic and vibrational decoupling. *Nat. Commun.* **2014**, *5*, No. 3252.
(52) Lu, C.; Yang, H.; Wang, J.; Tan, Q.; Fu, L. Utilization of iron tailings to prepare high-surface area mesoporous silica materials. *Sci. Total Environ.* **2020**, *736*, No. 139483.
(53) Guha, A.; Biswas, N.; Bhattacharjee, K.; Sahoo, N.; Kuotsu, K. pH responsive cylindrical MSN for oral delivery of insulin-design, fabrication and evaluation. *Drug Delivery* **2016**, *23*, 3552−3561.
(54) Taherzade, S. D.; Soleimannejad, J.; Tarlani, A. Application of Metal-Organic Framework Nano-MIL-100(Fe) for Sustainable Release of Doxycycline and Tetracycline. *Nanomaterials* **2017**, *7*, No. 215.